nature catalysis

ARTICLES

https://doi.org/10.1038/s41929-017-0016-y

Corrected: Publisher correction

Unravelling structure sensitivity in CO_2 hydrogenation over nickel

Charlotte Vogt[1], Esther Groeneveld[2], Gerda Kamsma[2], Maarten Nachtegaal[3], Li Lu[4], Christopher J. Kiely[4], Peter H. Berben[2], Florian Meirer[1] and Bert M. Weckhuysen[1*]

Continuous efforts in the field of materials science have allowed us to generate smaller and smaller metal nanoparticles, creating new opportunities to understand catalytic properties that depend on the metal particle size. Structure sensitivity is the phenomenon where not all surface atoms in a supported metal catalyst have the same activity. Understanding structure sensitivity can assist in the rational design of catalysts, allowing control over mechanisms, activity and selectivity, and thus even the viability of a catalytic reaction. Here, using a unique set of well-defined silica-supported Ni nanoclusters (1–7 nm) and advanced characterization methods, we prove how structure sensitivity influences the mechanism of catalytic CO_2 reduction, the nature of which has been long debated. These findings bring fundamental new understanding of CO_2 hydrogenation over Ni and allow us to control both activity and selectivity, which can be a means for CO_2 emission abatement through its valorization as a low- or even negative-cost feedstock on a low-cost transition-metal catalyst.

The reduction of CO_2 emissions into the Earth's atmosphere is gaining legislative importance in view of its impact on the climate[1–5]. Reduction of the harmful effect of these emissions through reclamation of CO_2 is made attractive because CO_2 can be a zero- or even negative-cost carbon feedstock[6,7]. The conversion of renewably produced hydrogen and CO_2 into methane, or synthetic natural gas, over Ni is a solution that combines the potential to reduce CO_2 emissions with a direct answer to the temporal mismatch in renewable electricity production capacity and demand[8–17]. Chemical energy storage in the form of hydrogen production by electrolysis is a relatively mature technology; however, the required costly infrastructure, and inefficiencies in distribution and storage deem it inconvenient for large-scale application in the near future. Point-source CO_2 hydrogenation to methane represents an alternative approach with higher energy density. Furthermore, methane is more easily liquefied and can be stored safely in large quantities through infrastructures that already exist[18,19]. Power-to-gas (in this case methane) is thus actively considered as being capable of balancing electric grid stability, which will allow us to increase the renewable energy supply[20].

The search for fossil fuel alternatives, and application of a process such as that described above can arguably be achieved only with the help of advances in catalysis and the closely related field of nanomaterials. Continuous efforts in both fields have allowed us to make increasingly smaller and catalytically more active (metal) particles. However, it is already known that making progressively smaller supported catalyst particles does not necessarily linearly correspond to higher catalytic activity[21–23]. This phenomenon, where not all atoms in a supported metal catalyst have the same activity, is called structure sensitivity and is often attributed to the distinctly different chemistries on different lattice planes for π-bond activation in CO_2, or σ-bond activation in, for example H_2 dissociation and C–H propagation[21,24]. The availability of stepped (less coordinated) versus terrace (more coordinated) sites on the surface of supported catalyst nanoparticles obviously changes with particle size, and atomic geometries become particularly interesting below 2 nm where, for example, π-bond activation is believed to not be able to occur[21]. While particle-size effects have been extensively studied for CO hydrogenation over Co[23,25], the understanding of such structure sensitivity effects for these critical smaller metal particle sizes is lacking as sub-2-nm particles prove difficult to synthesize for first-row transition metals (Co, Fe and Ni). However, a particle-size effect for CO_2 hydrogenation is much less well established[26].

Here, we used a unique set of SiO_2-supported Ni nanoparticles with diameters ranging from 1 to 7 nm in size, and show not only the existence of a distinct particle-size effect, but also evidence that allows us to understand the structure sensitivity of CO_2 hydrogenation over Ni as a model structure-sensitive reaction.

Classically, CO_2 hydrogenation over Ni is considered to follow a two-step, Langmuir–Hinshelwood-type mechanism, whereby first CO_2 dissociatively adsorbs with H_2 to form CO and H_2O in the reverse water gas shift (RWGS) reaction. The CO is then subsequently directly hydrogenated or dissociates to atomic C_{ads} and is then hydrogenated as schematically depicted in Fig. 1[6,7]. However, recent experimental and theoretical studies show that this reaction mechanism, particularly on surfaces of non-model catalysts, is not fully understood[27–32]. The RWGS reaction is believed to follow either of two mechanisms: the direct dissociation of CO_2 to CO via a CO_2^- ion (pathway 1 in Fig. 1), or a surface carbonate to formate reaction pathway (pathway 2 in Fig. 1). Much of the debate in the literature arises from the direct comparison between model and non-model surface studies. We hypothesize that mechanistic understanding of this reaction is closely related to its structure sensitivity.

An enhanced understanding of structure sensitivity and the mechanistic aspects behind this reaction will not only be a step towards a feasible method for the valorization of CO_2, with the potential to reduce its impact on the environment, but it will also aid in understanding similar structure-sensitive reactions. Evidence for the impact of different atomic coordinations in metal nanoclusters on the activation of different bond types, however, can have a far

[1]Inorganic Chemistry and Catalysis Group, Debye Institute for Nanomaterials Science, Utrecht University, Utrecht, The Netherlands. [2]BASF Nederland B.V., De Meern, The Netherlands. [3]Paul Scherrer Institute (PSI), Villigen PSI, Switzerland. [4]Department of Materials Science and Engineering, Lehigh University, Bethlehem, PA, USA. *e-mail: B.M.Weckhuysen@uu.nl

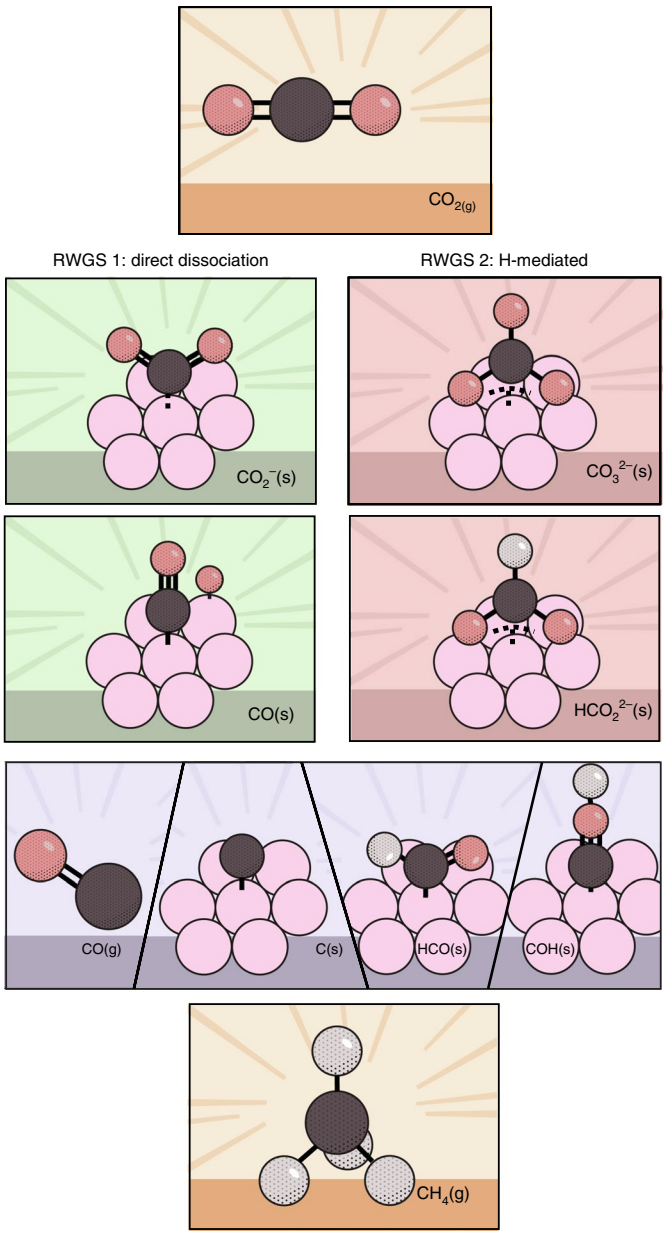

Fig. 1 | Mechanisms of catalytic CO_2 hydrogenation. A schematic overview of the mechanisms behind CO_2 hydrogenation as currently proposed in the literature, with simplification of certain non-rate-determining steps following the purple panels. Pathways 1 and 2, in the preceding green and red boxes, indicate reverse-water-gas-shift (RWGS) mechanisms. The depiction is simplified to merely top adsorption, but it is important to ascertain the coordination of Ni sites in each reaction step.

greater, multidisciplinary impact, as it will allow the rational design of catalysts enabling us to control, at the atomic level, the activity and selectivity of catalytic reactions[33–35]. It may even facilitate the discovery of new, previously unattainable catalytic reactions.

Results

Two separate particle-size-dependent mechanisms identified. A set of well-defined SiO_2-supported Ni catalysts was prepared by deposition precipitation, resulting in different nanoparticle sizes, ranging from 1 to 7 nm, by varying the weight loading of the precursor solutions. Particle sizes and oxidation states of fresh, reduced and spent catalysts were characterized by multiple techniques as summarized in Table 1; full details concerning the characterization methods and results can be found in the Supplementary Information (see 'Catalyst characterization' and 'Characterization results' sections of the Supplementary Information; Supplementary Figs. 1–14). The catalysts with different mean particle sizes were systematically tested in an operando transmission Fourier transform infrared (FT-IR) spectroscopy set-up, while recording online activity data. Figure 2 shows the observed activities towards methane formation in CO_2 hydrogenation with a 4:1 ratio of H_2/CO_2 at ambient pressure. The change in nanocluster size during the catalytic reaction was not significant, as evidenced by the post-reduction and spent structural characterization listed in Table 1 and Supplementary Fig. 9. The activity and turnover frequency (TOF) (Fig. 2b,c) were determined at 400 °C, and using particle sizes after reduction, as determined by high-angle annular dark-field scanning transmission electron microscopy (HAADF-STEM; Supplementary Fig. 7). Several additional trends serving to underwrite the attributed particle-size effects to surface-specific activity are reported in the Supplementary Information (see the Particle-size versus activity relationships section in the Supplementary Information and Supplementary Figs. 7–9). Furthermore, the experiments were repeated at 5 bar, 10 bar and 20 bar, and at 200 °C, 300 °C and 400 °C (Fig. 2e,f). In contrast to the extensively studied CO hydrogenation over Co (Fischer–Tropsch synthesis), where the TOF does not change for particle sizes larger than 6 nm[23,25], we observed a maximum activity at around 2.5 nm for CO_2 hydrogenation over Ni at 400 °C (Fig. 2b) and atmospheric pressure. Note that with increased pressure (Fig. 2e,f) the decrease in TOF for the smaller Ni nanoparticles is less evident.

We have hereby established a particle-size effect by use of a unique set of well-defined catalyst samples; that is, the surface-specific activity of catalytic CO_2 hydrogenation over Ni changes with Ni particle size. A trend is apparent throughout multiple experiments, and under different temperatures and pressures.

Operando spectroscopy was employed to relate these particle-size, or structure-sensitivity effects to surface species and processes. In Fig. 3a,b, difference FT-IR spectra are shown (that is, where the first spectrum of the series is subtracted from subsequent spectra). These consecutive spectra are focused on the absorption region between 2,250 and 1,400 cm^{-1}, where among other things intermediate C≡O to C–O stretching vibrations occur[36–39]. Furthermore, we also observe C–H stretching vibrations at 3,015 cm^{-1} for methane (Fig. 3c), and peaks at 1,932, 1,866 and 1,635 cm^{-1} for framework silica. All spectra were normalized to Ni surface area, and thus contain more intense silica peaks for samples with lower Ni wt%, as can be seen in Fig. 3a,b.

Three important reaction intermediates were observed with this type of analysis (Fig. 3d–f). The first such intermediate is CO_{ads} with peaks between 2,060 and 1,900 cm^{-1} where a distinction can be made between a set of peaks at 2,060 cm^{-1} with a shoulder at 2,019 cm^{-1}, and a peak at 1,903 cm^{-1} (Fig. 3e and Supplementary Fig. 10f–h). The former set describes terminally adsorbed CO atop a single Ni atom, for which vibrations can occur anywhere between 2,060 and 2,019 cm^{-1} depending on the oxidation state of Ni[36–39]. The band at 1,903 cm^{-1} is ascribed to bridged carbonyl species; more specifically, a CO species bound to three neighbouring Ni atoms. The second important reaction intermediate is gaseous CO, which gives a symmetrical broad band with maxima at 2,180 cm^{-1} and 2,095 cm^{-1} (Fig. 3d). Finally, a peak around 1,591 cm^{-1} is attributed to the third intermediate, namely surface formate (Fig. 3f, see also the FT-IR studies of catalyst samples section in the Supplementary Information). We have shown therefore that intermediates from RWGS pathway 1, as well as pathway 2 in Fig. 1, are both present on supported Ni catalysts. Figure 3a also already clearly demonstrates that the catalyst with the highest Ni dispersion shows relatively few bands ascribed to adspecies containing CO stretching vibrations,

Table 1 | Characteristics of the set of well-defined Ni/SiO_2 catalysts (A–H), listing their Ni loadings, and Ni particle sizes after reduction, and of spent catalysts as determined by TEM, HAADF-STEM, X-ray diffraction (XRD) and XAS

Sample[a]	Ni loading (wt%)	NiO TEM mean particle size spent (nm)[b]	Ni HAADF-STEM mean particle size after reduction (nm)[c]	Ni XAS coordination number (particle size) after reduction[50,51][d]	NiO XRD mean particle size after reduction (nm)[e]
A	1.0	1.1±0.4	1.8±0.8	6.4±1.2 (1 nm)	1.0±0.9
B	5.0	1.6±0.3	1.4±0.4	7.3±1.2 (2 nm)	2.0±0.5
C	4.7	1.6±0.7	1.2±0.5	7.1±1.5 (1.5 nm)	1.2±1.0
D	6.7	2.5±0.7	2.0±0.8	7.6±1.3 (2 nm)	0.9±0.2
E	1.7	2.6±0.5	1.4±0.4	5.8±3.1 (1 nm)	1.9±41
F	11.8	3.5±0.6	2.1±1.1	7.3±2.1 (2 nm)	2.3±1.2
G	19.5	5.0±1.4	4.4±2.4	7.4±1.3 (2 nm)	4.2±1.6
H	60.0	6.9±1.9	6.0±1.9	8.8±1.1 (6 nm)	5.2±2.6

[a]Arbitrary codes denoting the smallest (A) to largest (H) catalyst particle sizes as determined from the spent NiO particle sizes from TEM. [b]Average of at least 100 particles per sample, of spent samples. [c]Particle-size distributions determined after the reduction step (and re-oxidation by exposure to air) of at least 120 nanoparticles (see 'HAADF-STEM of post-reduction (Ni) particle sizes' in the Supplementary Methods for additional details on HAADF-STEM analysis). [d]XAS particle sizes (in brackets) determined from coordination numbers ex situ for particles after the respective reduction step (fit of first coordination shell)[50,51]. [e]Full-width at half-maximum XRD analysis of the average of the 52° and 74° diffraction peak of catalysts after the reduction step, and re-oxidation by exposure to air.

whereas for the catalyst with the largest Ni nanoparticles (Fig. 3b), the peaks in this region are more pronounced. This intriguing trend evolves progressively with increasing particle size, as shown in the Supplementary Information (see the FT-IR studies of catalyst samples section, Supplementary Fig. 17, and for experiments at 5, 10 and 20 bar, and 200, 300 and 400 °C, Supplementary Fig. 18), suggesting that with increasing Ni particle size pathway 1 becomes more dominant.

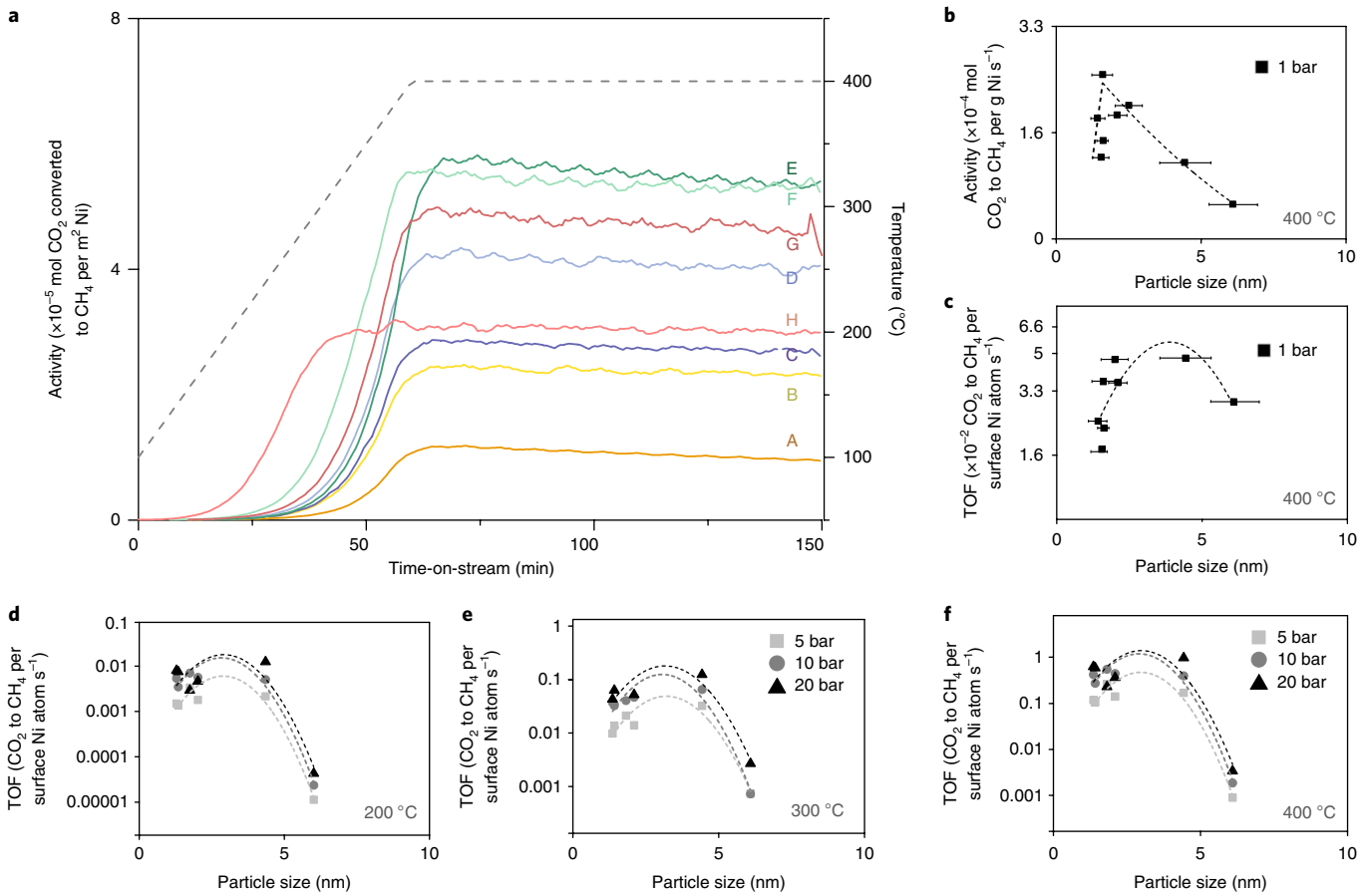

Fig. 2 | Particle size–activity relationships. a, Methane activity profiles normalized to Ni surface for catalyst samples A–H (see Table 1). The dashed grey line denotes the temperature profile; $H_2/CO_2 = 4$, 1 bar. **b**, The influence of Ni mean particle size on activity normalized to the Ni loading (400 °C, $H_2/CO_2 = 4$, 1 bar). Average TOF errors were found to be ±0.6%, and thus activity error bars lie within data markers. **c**, The influence of Ni mean particle size on the TOF in grey (400 °C, $H_2/CO_2 = 4$, 1 bar, assuming hemispherical particles and ten surface atoms per square nanometre). Horizontal error bars in **b** and **c** are taken as the standard deviation in Ni mean particle sizes determined by HAADF-STEM. **d**–**f**, The influence of Ni mean particle size on the TOF under different experimental conditions (5, 10 and 20 bar) at 200 °C (**d**), 300 °C (**e**) and 400 °C (**f**).

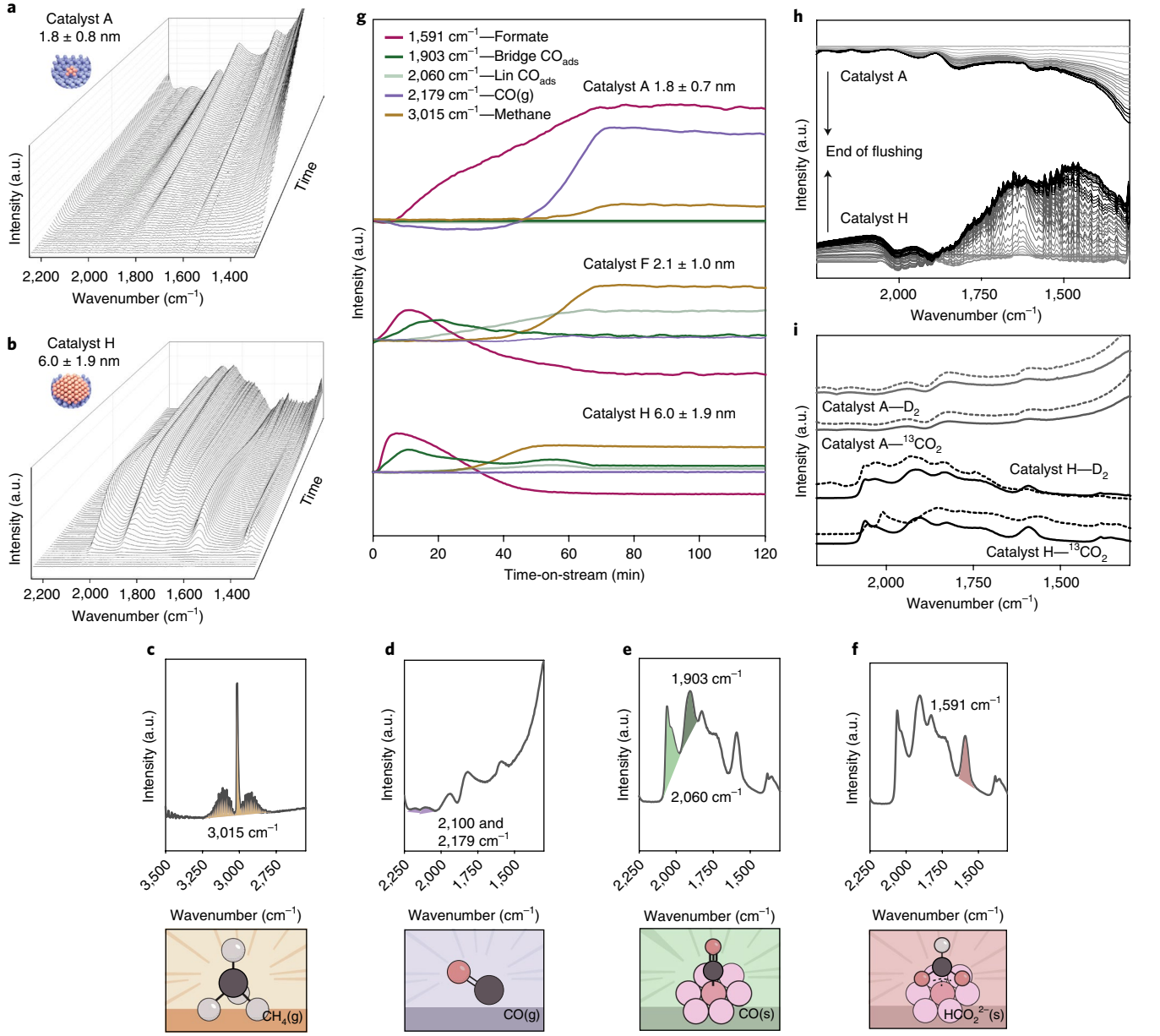

Fig. 3 | Combined operando FT-IR and catalyst activity measurements. a,**b**, Consecutive FT-IR spectra of the CO stretching absorption region plotted against time-on-stream for catalyst A (**a**) and catalyst H (**b**) at 400 °C and under atmospheric pressure. At 2,060 cm^{-1}, the C=O stretching vibrations are observed, ascribed to linearly/terminally adsorbed CO atop a single Ni atom. At 2,030 cm^{-1}, C=O stretching vibrations can be seen, ascribed to linearly/terminally adsorbed CO atop a single Ni(II) or Ni(III) atom. The peak at 1,918 cm^{-1} is attributed to bridged or three-fold carbonyl C=O stretching vibrations, existing only for the larger particle sizes but convoluted with SiO_2 framework stretching. The band at 1,847 cm^{-1} shows SiO_2 framework stretching vibration peaks, and the one at 1,591 cm^{-1} shows conjugated C-O/C=O stretching vibrations from formate species[36–39,52–56]. **c**-**f**, FT-IR spectra with highlighted peak areas for methane, gaseous CO, adsorbed CO and formate species. **g**, Integrated FT-IR peak areas as a function of time-on-stream. **h**, Consecutive operando FT-IR spectra recorded during post-reaction flushing with N_2 of the catalyst with the highest (catalyst A), and the lowest dispersion (catalyst H). **i**, Operando FT-IR spectra recorded during CO_2 hydrogenation experiments pulsed with labelled feedstocks. The solid lines denote non-pulsed feedstock, while the dashed lines denote a subsequent pulse of either $^{13}CO_2$ or D_2.

To assess the evolution of the FT-IR peaks during reaction, Fig. 3g shows integrated peak areas plotted against time-on-stream. Here it becomes evident that the intensity of the absorption bands in the CO_{ads} stretching region during CO_2 hydrogenation is positively correlated with, and therefore even an indirect measure for, mean catalyst particle size. Interestingly, the amount of gaseous CO seems negatively correlated with particle size and this species is observed only for the smallest Ni particles under investigation (< 1.5 nm); that is, those that show lower TOF values. Furthermore, with the knowledge that CO_{ads} atop a single nickel atom (2,060–2,019 cm^{-1}) has a weaker Ni–C bond than CO adsorbed in a tri-fold bridge position (1,903 cm^{-1}), these FT-IR results also give a first indication of the particle-size dependence of Sabatier's general principle for catalysis, where intermediate adsorption strength (in this case of CO) is required for optimal catalyst activity, which is achieved here by Ni particles with diameters in the 2–3 nm range. To corroborate this observation, the catalysts were flushed post reaction. As Fig. 3h shows,

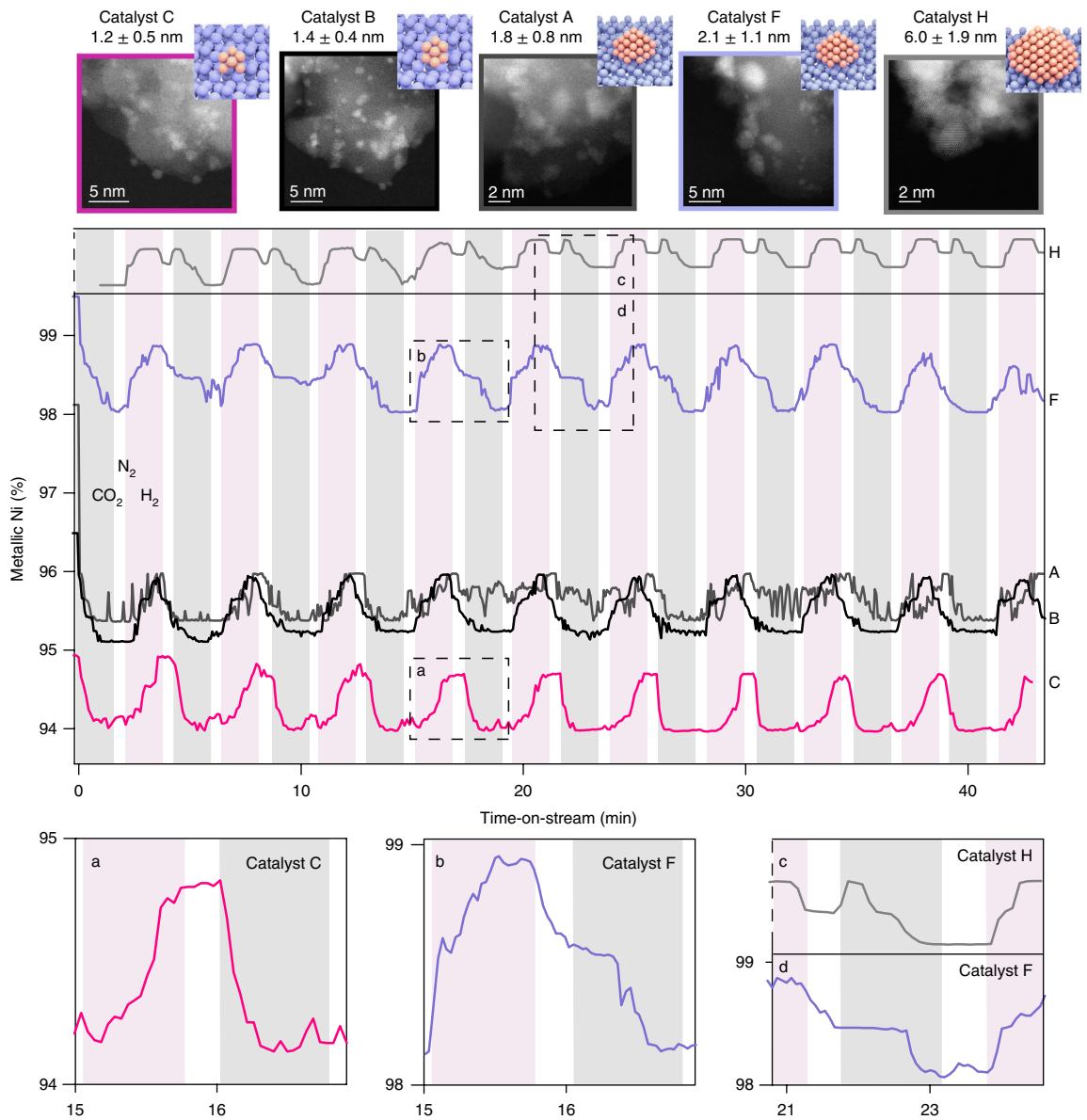

Fig. 4 | Q-XAS of five Ni/SiO_2 catalysts with different mean Ni particle sizes. Q-XAS allowed the determination of the percentage of metallic nickel with time-on-stream for different nickel nanoparticle sizes (see Table 1 for the characterization summary). Catalyst H was fitted with an ~30% NiO reference (as opposed to an 100% NiO reference for all other catalyst samples) to reveal the plotted profile from the highly metallic Ni spectra (see 'Operando quick XAS' section in the Supplementary Information). The bottom panels are magnifications of areas a-d in the middle panel.

any CO species on the small Ni particle sizes are easily flushed off, while for the large Ni particles the CO_{ads} is indeed present in a much more stable configuration, such as a bridged carbonyl, or carboxylate species.

While both RWGS pathways from Fig. 1 seem to occur, as both formate and $CO_{(ads)}$ species are observed in FT-IR, the intermediate species for each pathway show very different adsorption properties for the different particles sizes. Figure 3g shows that formate species are present irrespective of catalyst particle size; however, for the smaller Ni particle sizes, we see no decrease of the band during reaction as we do for larger Ni particle sizes. To assess whether both formate and CO species are still reactive, isotopically labelled gas feedstocks ($^{13}CO_2$ and D_2) were introduced. Interestingly, when pulsed with these labelled feedstocks, no interplay was observed between adsorbed ^{12}C, and H in the formate species and the isotopically labelled feedstocks for small Ni particle sizes. For the larger Ni particle sizes however, these labelled gases readily interacted and shifted the formate peak with both D_2 and $^{13}CO_2$ pulses at any given point in the reaction (Fig. 3i). While for the larger Ni nanoparticles intermediate CO_{ads} species dominate the surface, in the case of the smaller metal nanoparticle sizes formate species dominate and gaseous CO is also observed. The slow removal of oxygen-containing species has been suggested to be rate-limiting in transient studies[41]. From our results, it seems that this effect is amplified for smaller Ni nanoparticles. These findings are crucial for developing a mechanistic understanding of our observed structure-sensitivity effects.

Quick XAS explains observed structure-sensitivity effects. To further investigate the origin of the observed structure-sensitivity effects described above, we applied operando quick X-ray absorption spectroscopy (Q-XAS) with an effective time resolution of 4 s. To this end, 100 s CO_2 and H_2 gas pulses were alternated with 30 s N_2 pulses over the catalysts at 400, 350 and 300 °C.

These measurements were performed for the samples exhibiting the smallest catalyst particle sizes (A–C, 1.4–1.8 nm, 1–5% Ni loading), and samples with larger Ni particle size (F, 2–3 nm, 11.8% Ni loading, and H and G, 4.4 and 6.0 nm, and 19.5 and 60% Ni loading, respectively). Samples A, B and F were chosen because they showed sufficient X-ray absorption (that is, Ni weight loading), and because the particles on the catalysts were predominantly below 3 nm, which theoretically ensures > 35% surface atoms and thus sufficient signal in bulk Q-XAS to detect surface changes[42,43]. The larger particle sizes were chosen to verify observed trends. The 'Operando quick-XAS' section in the Supplementary Information describes in detail the clustering and least-squares fitting approach that we applied, which resulted in a quantitative value of Ni metal relative to NiO. The percentage of metallic nickel is plotted in Fig. 4, showing its evolution with time-on-stream.

The results of this operando spectroscopic characterization analysis are striking and it is worth highlighting that these experiments show exceptional sensitivity, as we are able to detect subtle surface oxidation state changes. First, without using a priori knowledge, we were able to distinguish the gas-flow pulse switches between feedstocks (CO_2 and H_2) in the oxidation state of the nickel. It is highly interesting that this method is thus sufficiently sensitive to detect 1–2% changes in oxidation state. A second striking observation is that for larger Ni particles there is a two-step re-oxidation (evidenced by plateaux in area c in Fig. 4) for subsequent CO_2 pulses. This suggests that, either with H_2 or with CO_{ads} on specific sites, a second, less preferred mechanism takes place for the RWGS reaction on larger particles that is slower and in which Ni has a higher overall oxidation state as in, for example, the less active pathway 2 in Fig. 1 where Ni with a higher oxidation state is inevitably formed. This plateau is much less apparent for catalysts with smaller Ni particle sizes that have fewer terrace sites. These results are in line with the assignment of more coordinatively saturated sites to the less active RWGS pathway 2 in Fig. 1. The initial oxidation and reduction observed during the N_2 pulses is caused by a residue of CO_2 or H_2 in the valve and lines after switching (see the Operando quick XAS section in the Supplementary Information). For the samples with smaller metal nanoparticles, it is clear that the removal of oxygen (or charged intermediates such as formate, as we know from FT-IR) is hampering activity. This is clearly evident by the difference in speed of oxidation versus reduction of the smaller versus the larger nanoparticles (area a versus area b in Fig. 4). This again underscores that the formate pathway (pathway 2 in Fig. 1) is not the most active pathway in RWGS and CO_2 hydrogenation.

The maximum change in degree of reduction for, for example, catalyst A is 2.3% (from 97.7 to 95.4%), while, for example, for catalyst sample F it is 1.5% (from 99.5 to 98.0%). It is important to evaluate the order of magnitude of these surface changes as they relate to the fraction of sites that are active in CO_2 activation. According to Supplementary Fig. 28 and the Quantification of active sites section in the Supplementary Information, a 1.4 nm particle should consist of around 192 Ni atoms, of which approximately 80% inhabit surface sites. Ideally, if all of these 153 surface atoms were active in just the activation of CO_2 during a pulse of CO_2, half of the surface atoms (~77 atoms) would be oxidized while the other half would be covered in CO_{ads}. A change in the reduction degree of the order of 1.5% corresponds to 3 atoms that are changing oxidation state, which means that around 4% of the surface atoms that can potentially be oxidized (~77 atoms) are actually oxidized. Applying this same reasoning to catalyst F gives us 6% of atoms that are active in CO_2 activation, or atoms that are part of active atomic coordinations in these particles. These small particle sizes are classically not even believed to be capable of activating π-bonds[21,22]. The maximum current model in (cobalt) face-centred-cubic nanoparticles gives a fraction of approximately 1% of these active B_5 sites for 1.2 nm particles[44]. This discrepancy gives us some important new insights into the likely restructuring effects exhibited by catalysts with such small Ni particle sizes, as we prove that the atomic coordinations that can cleave π-bonds are present (albeit in small quantities) under working conditions.

Discussion

Operando FT-IR spectroscopy measurements have shown that Ni/SiO_2 catalysts with larger Ni particle sizes retain several types of CO species with high surface coverage, while no gaseous CO is observed. The intensity of peaks in the CO_{ads} stretching region (2,060–1,600 cm^{-1}) is an indirect measure for Ni particle size. For the catalysts with high Ni dispersion, gaseous CO was observed, along with fewer adsorbed CO species. Clearly, the (re)activity, or stability of intermediate CO plays an important role in the observed Ni particle-size effects. Referring back to the first chemist who described the hydrogenation of CO_2, at first glance Sabatier's principle describes the CO intermediate effects we observe with FT-IR[6,7]. That is, the interactions between the catalyst and the substrate (CO_{ads}) should be just right, neither too strong, nor too weak. In essence, the larger Ni particles under observation are poisoned by a monolayer of CO_{ads} in a more stable bridge conformation, while the smallest Ni particles bind CO_{ads} too weakly, facilitating easy desorption. Catalysts facilitating the largest relative amount of linearly adsorbed CO show the highest activity. Thus, the rate-determining step in CO_2 hydrogenation is not the activation of CO_2 or the dissociation of CO, but rather relates to how easily the adsorbed intermediate CO species can be hydrogenated and the availability of adjacent H_{ads} sites to hydrogenate CO_{ads}. Furthermore, experiments at higher pressure show higher relative activity for smaller nanoparticles, which corroborates this hypothesis. Following this line of thought, activity should increase with smaller Ni particle size; however, this increased activity is likely to be hampered by the slow removal of oxidizing[41], or charged surface species in smaller nanoclusters, as shown by Q-XAS. By examining oxidation state changes with high-time-resolution XAS, complementing the results from operando FT-IR, we have identified the influence of more localized energy levels in the electronic band structure of smaller Ni nanoclusters ensuring increased stability of oxidizing or charged species. It is important to note here that it was previously suggested that particles smaller than 2 nm would not be able to cleave π-bonds, while we show experimentally that this is in fact not the case, as we observe gaseous CO and methane even with the smallest Ni particles[21]. These results allow us to discuss the mechanisms portrayed in Fig. 1, and point towards the direct dissociation of CO_2 (pathway 1) as the major active pathway in RWGS over Ni at 400 °C.

We are able to identify three probable contributions to the structure sensitivity of methanation over Ni catalysts. First, we show operando evidence for the presence of different sites with different activities within a narrow particle size distribution. Second, we show that at least for sub-2 nm Ni particles, current models for determining site fractions are not fully accurate and/or reactant-induced restructuring occurs. Finally, we present evidence that suggests that for sub-2-nm Ni particles, for example, the lower *d*-band energy or higher electron localization has a considerable impact on the catalytic activity as we observe increased stability of oxidizing or charged species on the surface.

We thus prove that structure-sensitivity effects are present in real catalysts and depend on a multitude of physical phenomena. Furthermore, it is implicit that model systems, such as single-crystal facet studies, will therefore lack the influence of electronic effects that can contribute to structure sensitivity. That is, it is important to study a model system that is dynamic, can restructure and in which the *d*-band energy or degree of electron (de-)localization can be examined (to also incorporate contributions from supports). Thus,

most importantly, we argue that structure sensitivity can currently be fully understood only in non-model catalysts.

Here, we have reported operando spectroscopic evidence for the effect of the Ni particle size on the stability and reactivity of intermediates in CO_2 methanation over Ni, which serves to provide a mechanistic understanding of how to control the activity of this reaction. Furthermore, these results provide new found potential for the use of Ni in Fischer–Tropsch synthesis, which is often neglected as an industrially relevant FT catalyst due to the assumed formation of highly toxic nickel tetracarbonyls, which were not found to be present in our study. We show decreasing CO adsorption strength with decreasing particle size. As the adsorption strength of CO is directly related to the formation of $Ni(CO)_4$, we postulate that under the condition that the particles remain structurally stable, Ni particles of optimal size may find revived interest for Fischer–Tropsch synthesis as highly selective C_{5+} catalysts, on reducible supports[45,46]. The current operando spectroscopy study can be regarded not only as a major step forward in understanding the origin of Ni particle-size effects in CO_2 hydrogenation and activation, but it also shines a light on the reactivity of intermediate CO with direct practical interest, for example, in the Fischer–Tropsch synthesis of hydrocarbons. The analogous methodologies developed here also provide a fundamental insight into the performance–size relationship for CO_2 hydrogenation and, consequently, may be more generally applicable for studies of metal nanoparticle-size effects.

Methods

Catalyst synthesis. Silica-supported Ni nanoparticles were made by homogeneous deposition precipitation (HDP), and co-precipitation according to previous studies[46–48]. For catalysts A–G, prepared by HDP, different weight loadings (1–20%) of Ni precursor were dissolved in water, in which silica was suspended. The pH was increased under continuous stirring by addition of an alkaline solution. Catalyst H was made by co-precipitation of $NiCO_3$ with silica precursor in solution, precipitation was induced by the addition of NaOH. The catalyst samples under investigation have varying Ni mean particle sizes, as listed in Table 1.

Catalyst characterization. Temperature-programmed reduction (TPR) was performed in a Tristar II series analyser. The middle of the second reduction peak (Ni(II) to Ni(0)) was chosen as the reduction temperature for each catalyst. According to these results, all reduction steps in this work were ramped at 5 °C min^{-1} to 600 °C (catalyst A), 550 °C (catalyst B–G) and 500 °C (catalyst H), and held at these respective temperatures for 30 min. The oxidation states of the catalysts after this procedure were examined by X-ray absorption spectroscopy, and found to be in a fully reduced condition prior to activity experiments (see the Characterization results section in the Supplementary Information).

Materials for examination by scanning transmission electron microscopy (STEM) were dry-dispersed onto a holey carbon TEM grid. The catalyst samples were examined using bright-field- and high-angle annular dark-field STEM imaging mode in an aberration-corrected JEOL ARM-200CF scanning transmission electron microscope operating at 200 kV. This microscope was also equipped with a Centurio silicon drift detector system for X-ray energy dispersive spectroscopy analysis.

Furthermore, fresh, reduced and passivated, and spent samples were examined with transmission electron microscopy (TEM) in an FEI Tecnai12 operated at 120 kV or in an FEI Tecnai20F operated at 200 kV. Samples were crushed and suspended in ethanol under ultrasonic vibration. A drop of this suspension was deposited onto a holey carbon film on a 300 mesh copper grid. Metal and metal oxide particle sizes quoted in Table 1 are length–number mean diameters (> 100 particles). Particle-size distributions were determined by TEM for fresh, reduced (and reoxidized) and spent samples (see the Characterization results section in the Supporting information). X-ray diffraction measurements of fresh, reduced (and re-oxidized) and spent samples were also carried out in a Bruker D2 Phaser to determine crystallite size.

Operando FT-IR with on-line product analysis. Operando Fourier transform infrared (FT-IR) spectroscopy measurements were performed to study reactants, intermediates and products in CO_2 hydrogenation over Ni. Product formation was followed by on-line gas chromatography. Time-resolved operando FT-IR spectra were recorded to study the effect of different mean particle sizes on reaction intermediates and catalyst activity at different temperatures. The operando FT-IR measurements were carried out using a Bruker Tensor 37 FT-IR spectrometer equipped with a DTGS detector. Spectra were recorded every 30 s for each experiment. On-line product analysis was performed with an Interscience custom-built Global Analyzer Solutions Compact $GC_{4.0}$ gas chromatograph with a time resolution of around 10 s for lower hydrocarbons (methane, ethane and ethene). The CO_2 hydrogenation experiments were carried out in a Specac high-temperature transmission IR reaction cell (as depicted in Supplementary Fig. 1). To this end, the catalyst powders were pressed into wafers of approximately 16 mm in diameter, and around 0.1 mm thickness weighing between 10 and 15 mg. These self-supported catalyst wafers were created using a Specac laboratory pellet press, a diaphragm vacuum pump and around 4 t of pressure. Before each reaction, each catalyst was reduced at a temperature pre-determined by TPR, and reduced in situ with a 5 °C min^{-1} temperature ramp, and a 3 min hold in a 1:1, N_2/H_2 flow with a total of 25 ml min^{-1} (both Linde, 4.9). After this in situ reduction treatment, the temperature of the reaction cell was brought to 100 °C, and the reactants were introduced through Bronkhorst EL-FLOW mass flow controllers; CO_2 at 1.25 ml min^{-1}, H_2 at 5 ml min^{-1} and N_2 to dilute at 6.25 ml min^{-1} for a total flow of 12.5 ml min^{-1}. In a TPR, the reactor was heated at a ramp rate of 5 °C min^{-1} to 400 °C, where eventually the temperature was held for 90 min. For each catalyst sample with differing metal dispersion, on-line activity data were collected with a time resolution of 30 s. Simultaneously, successive operando FT-IR spectra were also recorded with a time resolution of 30 s (see the FR-IR studies of catalyst samples section in the Supplementary Information).

Operando quick XAS with on-line product analysis. Operando X-ray absorption spectroscopy (and ex situ characterization) with millisecond time resolution was performed at the SuperXAS beamline (X10DA) at the Swiss Light Source in transmission mode. The X-ray beam from the bending magnet was monochromatized with a Si(111) channel-cut crystal in the QuickXAS monochromator. The Si(111) crystal was rotated at a frequency of 10 Hz across the Ni K-edge, and the signals of the ionization chambers and the angular encoder were sampled at a frequency of 2 MHz. The edge energy was calibrated using a Ni foil. The measurements were performed in a custom-built operando reaction cell, which is described in more detail in the Supplementary Information (see the Operando quick XAS section). Q-XAS data were evaluated using the JAQ Analyzes QEXAFS version 3.3.53 software and a self-developed Matlab code was used for principal component analysis and subsequent clustering[50]. Least-squares linear combination fitting of clustered spectra was performed using the Athena software[51]. On the basis of the signal-to-noise ratio, the data were binned to an effective time resolution of 4 s. Further information about the Q-XAS data processing can be found in the Supplementary Information (see the Operando quick XAS and Quantification of Q-XAS results sections).

Data availability. The data that support the plots within this paper and other findings of this study are available from the corresponding author upon reasonable request.

Received: 1 June 2017; Accepted: 23 November 2017;
Published online: 29 January 2018

References

1. *Adoption of the Paris Agreement* FCCC/CP/2015/L.9/Rev.1 (UNFCCC, 2015).
2. McGlade, C. & Ekins, P. The geographical distribution of fossil fuels unused when limiting global warming to 2 °C. *Nature* **517**, 187–190 (2015).
3. Ertl, G., Knözinger, H. & Weitkamp, J. (eds) *Handbook of Heterogeneous Catalysis* (Wiley VCH, Weinheim, 1997).
4. Ertl, G. Reactions at surfaces: From atoms to complexity (Nobel lecture). *Angew. Chem. Int. Ed.* **47**, 3524–3535 (2008).
5. Somorjai, G. A. & Li, Y. *Introduction to Surface Chemistry and Catalysis* (John Wiley & Sons, New York, 2010).
6. Senderens, J.-B. & Sabatier, P. Nouvelles synthèses du méthane. *Compt. Rend.* **82**, 514–516 (1902).
7. Sabatier, P. & Senderens, J.-B. Hydrogénation directe des oxydes du carbone en présence de divers métaux divisés. *Compt. Rend.* **134**, 689–691 (1903).
8. Armstrong, R. C. et al. The frontiers of energy. *Nat. Energy* **1**, 15020 (2016).
9. Hull, J. F. et al. Reversible hydrogen storage using CO_2 and a proton-switchable iridium catalyst in aqueous media under mild temperatures and pressures. *Nat. Chem.* **4**, 383–388 (2012).
10. Studt, F. et al. Discovery of a Ni-Ga catalyst for carbon dioxide reduction to methanol. *Nat. Chem.* **6**, 320–324 (2014).
11. Schuchmann, K. & Muller, V. Direct and reversible hydrogenation of CO_2 to formate by a bacterial carbon dioxide reductase. *Science* **342**, 1382–1386 (2013).
12. Rostrup-Nielsen, J. R., Pedersen, K. & Sehested, J. High temperature methanation - sintering and structure sensitivity. *Appl. Catal. A* **330**, 134–138 (2007).
13. Silaghi, M., Comas-Vives, A. & Copéret, C. CO_2 activation on Ni/γ−Al_2O_3 catalysts by first-principles calculations: from ideal surfaces to supported nanoparticles. *ACS Catal.* **6**, 4501–4505 (2016).
14. Kopyscinski, J., Schildhauer, T. J. & Biollaz, S. M. A. Production of synthetic natural gas (SNG) from coal and dry biomass—a technology review from 1950 to 2009. *Fuel* **89**, 1763–1783 (2010).

15. Yan, Z., Ding, R., Song, L. & Qian, L. Mechanistic study of carbon dioxide reforming with methane over supported nickel catalysts. *Energy Fuels* **12**, 1114–1120 (1998).
16. Lewis, N. S. & Nocera, D. G. Powering the planet: chemical challenges in solar energy utilization. *Proc. Natl Acad. Sci. USA* **104**, 15729–15735 (2007).
17. Steinfeld, A. Solar thermochemical production of hydrogen—a review. *Sol. Energy* **78**, 603–615 (2005).
18. Centi, G. & Perathoner, S. Opportunities and prospects in the chemical recycling of carbon dioxide to fuels. *Catal. Today* **148**, 191–205 (2009).
19. Tada, S., Shimizu, T., Kameyama, H., Haneda, T. & Kikuchi, R. Ni/CeO_2 catalysts with high CO_2 methanation activity and high CH_4 selectivity at low temperatures. *Int. J. Hydrog. Energy* **37**, 5527–5531 (2012).
20. Schlögl, R. The revolution continues: Energiewende 2.0. *Angew. Chem. Int. Ed.* **54**, 4436–4439 (2015).
21. van Santen, R. A. Complementary structure sensitive and insensitive catalytic relationships. *Acc. Chem. Res.* **42**, 57–66 (2009).
22. van Hardeveld, R. & van Montfoort, A. The influence of crystallite size on the adsorption of molecular nitrogen on nickel, palladium and platinum. *Surf. Sci.* **4**, 396–430 (1966).
23. Bezemer, G. L. et al. Cobalt particle size effects in the Fischer−Tropsch reaction studied with carbon nanofiber supported catalysts. *J. Am. Chem. Soc.* **128**, 3956–3964 (2006).
24. Ren, J. et al. Insights into the mechanisms of CO_2 methanation on Ni(111) surfaces by density functional theory. *Appl. Surf. Sci.* **351**, 504–516 (2015).
25. den Breejen, J. P. et al. On the origin of the cobalt particle size effects in Fischer–Tropsch catalysis. *J. Am. Chem. Soc.* **131**, 7197–7203 (2009).
26. Iablokov, V. et al. Size-controlled model Co nanoparticle catalysts for CO_2 hydrogenation: synthesis, characterization, and catalytic reactions. *Nano Lett.* **12**, 3091–3096 (2012).
27. Heine, C., Lechner, B. A. J., Bluhm, H. & Salmeron, M. Recycling of CO_2: probing the chemical state of the Ni(111) surface during the methanation reaction with ambient-pressure X-ray photoelectron spectroscopy. *J. Am. Chem. Soc.* **138**, 13246–13252 (2016).
28. Czekaj, I., Loviat, F., Raimondi, F., Biollaz, S. & Wokaun, A. Characterization of surface processes at the Ni-based catalyst during the methanation of biomass-derived synthesis gas: X-ray photoelectron spectroscopy (XPS). *Appl. Catal. A* **329**, 68–78 (2007).
29. Marwood, M., Doepper, R. & Renken, A. In-situ surface and gas phase analysis for kinetic studies under transient conditions. The catalytic hydrogenation of CO_2. *Appl. Catal. A* **151**, 223–246 (1997).
30. Tao, F. et al. Reaction-driven restructuring of Rh-Pd and Pt-Pd core-shell nanoparticles. *Science* **322**, 932–934 (2008).
31. Tao, F. et al. Break-up of stepped platinum catalyst surfaces by high CO coverage. *Science* **327**, 850–853 (2010).
32. Miao, D. et al. Water-gas shift reaction over platinum/strontium apatite catalysts. *Appl. Catal. B* **202**, 587–596 (2017).
33. Lamberti, C., Zecchina, A., Groppo, E. & Bordiga, S. Probing the surfaces of heterogeneous catalysts by in situ IR spectroscopy. *Chem. Soc. Rev.* **12**, 4951–5001 (2010).
34. Yardimci, D., Serna, P. & Gates, B. C. Surface-mediated synthesis of dimeric rhodium catalysts on MgO: Tracking changes in the nuclearity and ligand environment of the catalytically active sites by X-ray absorption and infrared spectroscopies. *Chem. Eur. J.* **19**, 1235–1245 (2013).
35. Kalz, K. F. et al. Future challenges in heterogeneous catalysis: understanding catalysts under dynamic reaction conditions. *ChemCatChem* **9**, 17–29 (2017).
36. Camputano, J. C. & Greenler, R. G. The adsorption sites of CO on Ni(111) as determined by infrared reflection-absorption spectroscopy. *Surf. Sci.* **83**, 301–312 (1979).
37. Trenary, M., Uram, K. J. & Yates, J. T. An infrared reflection-absorption study of CO chemisorbed on clean and sulfided Ni(111)—evidence for local surface interactions. *Surf. Sci.* **157**, 512–538 (1985).
38. Layman, K. A. & Bussell, M. E. Infrared spectroscopic investigation of CO adsorption on silica-supported nickel phosphide catalysts. *J. Phys. Chem. B* **108**, 10930–10941 (2004).
39. Courtois, M. & Teichner, S. J. Infrared studies of CO, O_2 and CO_2 gases and their interaction products, chemically adsorbed on nickel oxide. *J. Catal.* **135**, 121–135 (1962).
40. Vesselli, E., Schweicher, J., Bundhoo, A., Frennet, A. & Kruse, N. Catalytic CO_2 hydrogenation on nickel: novel insight by chemical transient kinetics. *J. Phys. Chem. C.* **115**, 1255–1260 (2011).
41. van Bokhoven, J. A. & Lamberti, C. (eds) *X-Ray Absorption and X-Ray Emission Spectroscopy: Theory and Applications* (John Wiley & Sons, New York, NY, 2016).
42. Bordiga, S., Groppo, E., Agostini, G., Van Bokhoven, J. A. & Lamberti, C. Reactivity of surface species in heterogeneous catalysts probed by in situ X-ray absorption techniques. *Chem. Rev.* **113**, 1736–1850 (2013).
43. Van Helden, P., Ciobica, I. M. & Coetzer, R. L. J. The size-dependent site composition of FCC cobalt nanocrystals. *Catal. Today* **261**, 48–59 (2016).
44. Enger, B. C. & Holmen, A. Nickel and Fischer-Tropsch synthesis. *Catal. Rev. Sci. Eng.* **54**, 437–488 (2012).
45. Munnik, P., Velthoen, M. E. Z., de Jongh, P. E., De Jong, K. P. & Gommes, C. J. Nanoparticle growth in supported nickel catalysts during methanation reaction-larger is better. *Angew. Chem. Int. Ed.* **53**, 9493–9497 (2014).
46. Ermakova, M. A. & Ermakov, D. Y. High-loaded nickel-silica catalysts for hydrogenation, prepared by sol-gel route: structure and catalytic behavior. *Appl. Catal. A* **245**, 277–288 (2003).
47. De Jong, K. P. in *Synthesis of Solid Catalysts* (ed. De Jong, K. P.) 111–134 (Wiley-VCH Verlag, Weinheim, 2009).
48. Lok, M. in *Synthesis of Solid Catalysts* (ed. De Jong, K. P.) 135–151 (Wiley-VCH Verlag, Weinheim, 2009).
49. Liu, Y. et al. TXM-Wizard: A program for advanced data collection and evaluation in full-field transmission X-ray microscopy. *J. Synchrotron. Radiat.* **19**, 281–287 (2012).
50. Ravel, B. & Newville, M. ATHENA, ARTEMIS, HEPHAESTUS: data analysis for X-ray absorption spectroscopy using IFEFFIT. *J. Synchrotron. Radiat.* **12**, 537–541 (2005).
51. Frenkel, A. I., Hills, C. W. & Nuzzo, R. G. A view from the inside: complexity in the atomic scale ordering of supported metal nanoparticles. *J. Phys. Chem. B* **105**, 12689–12703 (2001).
52. Chukin, G. D. & Malevich, V. I. Infrared spectra of silica. *Zhurnal Prikl. Spektrosk.* **26**, 223–229 (1977).
53. Socrates, G. *Infrared and Raman Characteristic Group Frequencies* (Wiley, Chichester, 2001).
54. Erley, W., Wagner, H. & Ibach, H. Adsorption sites and long range order —vibrational spectra for CO on Ni(111). *Surf. Sci.* **80**, 612–619 (1979).
55. Erley, W. & Wagner, H. Thermal decomposition of CO on a stepped Ni surface. *Surf. Sci.* **74**, 333–341 (1978).
56. Chumakova, A. V. et al. Periodic order and defects in Ni-based inverse opal-like crystals on the mesoscopic and atomic scale. *Phys. Rev. B* **90**, 1–9 (2014).

Acknowledgements

The authors thank NWO and BASF for a TA-CHIPP grant. B.M.W. also thanks NWO for a Gravitation programme (Netherlands Center for Multiscale Catalytic Energy Conversion (MCEC)). Furthermore, S. Parker and J. Palle (Utrecht University, UU) are acknowledged for their contributions in measuring FT-IR spectra and activity data. F. Soulimani (UU) and P. de Peinder (UU) are acknowledged for discussions regarding FT-IR data. J. Geus (UU) is also acknowledged for fruitful discussions. A. van der Eerden, M. Filez and H. Schaink, all from UU, are acknowledged for (technical) support in measuring XAS. O. Sofanova (PSI) is thanked for reading the manuscript carefully prior to submission.

Author contributions

E.G. made the set of catalyst samples. C.V., F.M. and B.M.W. conceived and designed the operando experiments. C.V. performed the operando spectroscopic experiments. FT-IR data analysis was performed by C.V. with input from B.M.W., while quick XAS data analysis was performed by F.M. and C.V. L.L. and C.J.K performed and interpreted HAADF–STEM measurements; G.K., E.G. and P.H.B. performed and interpreted H_2 chemisorption measurements and prepared reference XAS samples. M.N. aided in the set-up, and provided support with the operando quick XAS measurements. C.V., F.M. and B.M.W. wrote the paper. All authors discussed the results and commented on the manuscript.

Competing interests

The authors declare no competing financial interests.

Additional information

Supplementary information is available for this paper at https://doi.org/10.1038/s41929-017-0016-y.

Reprints and permissions information is available at www.nature.com/reprints.

Correspondence and requests for materials should be addressed to B.M.W.

Publisher's note: Springer Nature remains neutral with regard to jurisdictional claims in published maps and institutional affiliations.